



Cite this: DOI: 10.1039/c8nj02786b

Synthesis and functionalization of ordered mesoporous carbons supported Pt nanoparticles for hydroconversion of *n*-heptane†

S. Said 

A comprehensive study was performed on the spectroscopic and textural properties of ordered mesoporous carbon (OMC) of the CMK-3 type modified by acid oxidation using $K_2S_2O_8$ as a benign oxidant and nitrogen-doping by the aid of the polymerization of ethylenediamine and carbon tetrachloride inside the pore channels of SBA-15 hard template. The pristine, nitrogen-doped, and oxidized-ordered mesoporous carbons were used as supports to prepare 10 wt% platinum nanoparticles-loaded catalysts using ethylene glycol as a reducing agent. The catalytic behavior, mechanism, and influence of the surface functionalization of the ordered mesoporous carbon bifunctional catalysts toward the hydroconversion of *n*-heptane using a fixed-bed flow system operated under atmospheric pressure were investigated. The synthesized samples were characterized by various analytical and spectroscopic techniques. The mesostructural regularity corresponding to the hexagonal $P6mm$ symmetry of the OMC-CMK-3 type was well-reserved even after surface modifications replicated from an SBA-15 template. H_2 pulse chemisorption and EDX mapping images confirmed differences in the Pt NPs contents and dispersion depending on the support composition. The catalytic activity results achieved were hand in hand with the proper balance between the acidity strength and Pt NPs dispersion degree.

Received 5th June 2018,
Accepted 24th July 2018

DOI: 10.1039/c8nj02786b

rsc.li/njc

1. Introduction

Crude oil is a complex mixture made up of many thousands of different molecules, and its natural state at the wellhead actually has limited value. A series of complex and expensive industrial processes are thus needed to convert the crude oil into a useful range of different products. Alkylation, reforming, isomerization, thermal, catalytic, and hydrocracking are the typical chemical processing steps that are combined together to constitute petroleum refining of the various streams coming from the distillation units. Therefore, the aim of crude oil refining is to reduce the volume of low value products and to ensure that as much value can be created from the remaining marketable production. In order to enhance the octane level of gasoline and to improve the low-temperature performance of diesel or lubricating oils, branched alkane isomers are some of the more desirable components.¹ *n*-Paraffin hydroisomerization is commonly conducted over bifunctional catalysts consisting of a hydrogenation/dehydrogenation function performed by a noble metal (Pt or Pd) supported on a support having acid sites for skeletal isomerization reaction.²

Ordered mesoporous carbon (OMC) has attracted substantial research enthusiasm as a novel class of carbonaceous material since it was first synthesized by Ryoo in 1999.³ OMC materials hold great potential to be applied for catalysis,⁴ electrochemistry,⁵ and adsorption⁶ owing to their unique structural properties, such as large specific surface area, ordered channels, uniform pore size, and mechanical and thermal stability. Ordered mesoporous carbons (OMCs) can be synthesized *via* two routes based on template carbonization. The first one is called the 'hard-templating' or 'nanocasting' multi-step route; in which the ordered mesoporous silica serves as a hard template, which is impregnated with an appropriate carbon precursor (*e.g.*, sucrose), carbonized, and finally the silica is removed by dissolving in HF. Such treatment results in a porous carbon material as a reverse replica of the silica template.⁷ The second method called 'soft-templating' is a one-step method, where triblock copolymers act as the template. The interactions between a triblock copolymer and polymeric carbon precursor and further heating result in degradation of sensitive copolymer molecules, obtaining ordered mesoporous carbon.⁸ However, the relatively inert nature and lack of functional groups on the surface of pristine OMC materials limit their practical applications. Many studies have been carried out to find methods for the modification and functionalization of OMC materials.⁹ Among these, post-synthesis acid oxidation has been recognized as an effective way to introduce large amounts of

Refining Department, Catalysis Division, Egyptian Petroleum Research Institute, Nasr City, Cairo 11727, Egypt. E-mail: ssm_epri83@yahoo.com

† Electronic supplementary information (ESI) available. See DOI: 10.1039/c8nj02786b

oxygen-containing functional groups to the carbonaceous surface,¹⁰ and heteroatom doping is also widely applied; for example, the doping of nitrogen has a considerable effect on carbon by adjusting the geometric/electronic structure, altering the physical and chemical properties, especially the hydrophilicity of the OMC materials and the basicity, therefore enhancing the catalytic properties of the carbon materials.¹¹ Meanwhile, a carbonaceous surface enriched with heteroatom functional groups can be applied as a versatile platform for further modifications.¹² Nonetheless, functionalization of the carbon surface can definitely generate some problems too, such as structural damage and an uneven distribution of the surface functional groups.¹³

Noble metal nanoparticles (NPs) are the most widely applied NPs in catalysis owing to their high activity and selectivity for many chemical reactions.¹⁴ Specifically, the Pt noble metal, besides its hydrogenating/dehydrogenating function, has shown outstanding catalytic performance as it can help alleviate bifunctional catalyst deactivation by hydrogenating coke precursors during the petrochemical hydroconversion reaction.¹⁵ Further, downsizing Pt NPs increases their specific surface area, thus providing more active sites for catalytic reactions. Solvothermal approaches using ethylene glycol as the reducing agent are frequently employed for the anchoring of Pt nanoparticles on to carbons.¹⁶

Fernandes and coworkers¹⁷ used the Pt/CMK-3 catalyst, and for comparison a commercial carbon surface supplied by NORIT (GL-50), as a support but in order to increase its surface acidity, it was submitted to wet oxidation with 21 and 65 wt% HNO₃ solutions. The Pt/CMK-3, Pt/(GL-50)(21) and Pt/(GL-50)(65) catalysts were tested for the hydroisomerization of *n*-decane and the results showed identical conversions (8–10%) and product distribution in the studied temperature range with a selectivity greater than 70% toward the formation of isomerization products.

The aim of the present research was to perform a comprehensive study on the textural and morphological properties of the functionalized ordered mesoporous carbon surface both from nitrogen-doping and by post-synthesis acid oxidation and to investigate the influence of the surface modification potentialities as supports in the performance of Pt NPs/pristine, oxidized, and nitrogen-functionalized OMCs as bifunctional catalysts for *n*-heptane hydroconversion under atmospheric pressure using a fixed-bed flow system. To date the testing of functionalized surface ordered mesoporous carbons in the hydroconversion of *n*-heptane has not been reported, as far as we know, despite the advantageous properties of ordered mesoporous carbon materials. Thus, this is to the best of the author's knowledge, the first reported study investigating the use of surface functionalized ordered mesoporous carbon materials for this particular catalytic reaction.

2. Experimental

2.1. Mesoporous silica SBA-15 preparation

The mesoporous silica SBA-15 was used as a hard template for the synthesis of the ordered mesoporous carbon of the type CMK-3.

The SBA-15 was prepared in a two-step pathway using tetraethylthosilicate (TEOS, Aldrich) as the silica source and a nonionic surfactant ((EO)₂₀(PO)₇₀(EO)₂₀, Aldrich) following the procedure described by Zhao *et al.*¹⁸ Briefly, 4 g of pluronic 123 was dissolved in 30 g of distilled water and 120 g of 2 M HCl solution with stirring at 40 °C. Then, 8.50 g of tetraethylthosilicate (TEOS, Aldrich) was added into that solution with stirring at 40 °C for 20 h, followed by aging at 90 °C overnight without stirring. A white precipitate was recovered by filtration and air-dried for 24 h. The template was removed from the as-synthesized mesoporous material by calcination at 500 °C for 6 h (heating rate = 1 °C min⁻¹).

2.1.2. Synthesis of pristine, oxidized, and nitrogen-functionalized OMCs. (a) OMC-CMK-3 was synthesized by nanocasting the SBA-15 template using sucrose as the carbon precursor following the method described by Vinu *et al.*¹⁹ In short, about 0.9 g of sucrose (Sigma, 99.5%) was dissolved in 0.1 g H₂SO₄ acid added drop wise to 1.0 g of SBA-15 under stirring. The paste-like mixture was heated in an oven at 100 °C for 6 h and then the temperature was subsequently increased to 160 °C and maintained there for another 6 h. The brownish powder corresponding to the sucrose/silica composite was again impregnated with (0.75 g sucrose, 0.084 g concentrated H₂SO₄, and 5 g H₂O) and heated as indicated before. The resulting black powder was then calcined in a tubular furnace at 900 °C for 5 h under a N₂ atmosphere. The pitch black carbon sample was treated with 5 wt% of HF (48%) to remove the silica template and washed 3 times with excess ethanol and then dried at 100 °C for 6 h in an oven. The obtained carbon sample was donated as pristine-ordered mesoporous carbon (P-OMC).

(b) Oxidized-OMC was prepared following the method described by Barczak *et al.*¹⁰ First, 1.0 g pristine OMC was put into a beaker filled with 1.75 M solution of potassium persulfate (KPS, 97%, CDH) in 2 M sulfuric acid (50 mL) and stirred for 24 h at RT. After that, the mixture was filtrated and washed with water and ethanol. A black solid was obtained after drying at 80 °C overnight. This oxidized sample is abbreviated herein as O-OMC.

(c) Nitrogen-functionalized OMC along with the aid of ethylenediamine (EDA) and carbon tetrachloride (CTC) as precursors²⁰ was prepared as follows: SBA-15 (0.5 g) was well stirred with a mixture containing EDA (1.35 g) and CTC (3 g); the mixture was refluxed under stirring at 90 °C for 6 h. The resultant dark brown colored composite material was dried at 100 °C for 12 h. The obtained material was pyrolyzed at 600 °C (heating rate 3.0 °C min⁻¹) under nitrogen flow (50 mL min⁻¹) for 5 h. The carbonized material was treated with 5 wt% hydrofluoric acid to dissolve the silica framework and the ordered mesoporous carbon nitride was recovered by filtration, followed by washing several times with ethanol and then drying at 100 °C. This sample is abbreviated herein as N-OMC.

2.1.3. Preparation of Pt/OMCs catalysts. Pt nanoparticles (Pt NPs) were loaded on the P-, O-, and N-OMCs by the aid of an ethylene glycol (EG) reduction method.²¹ Here, 250 mg of the OMCs was suspended in 25 mL EG under ultrasonic stirring for 40 min. A given amount of the H₂PtCl₆/EG solution (Pt: 3.7 mg mL⁻¹) was added in order to obtain the Pt/OMCs

(pristine, oxidized, and *N*-functionalized) with 10 wt% metal loading. Then, the pH of the solution was adjusted to 13 by adding NaOH, followed by heating at 130 °C for 3 h under flowing Ar. After cooling down to the room temperature, the pH of the mixture was adjusted to 2 by adding 1.0 M HCl aqueous solution, which was then stirred for another 2 h to ensure that the Pt NPs were fully loaded on to the ordered mesoporous carbons. Finally, the powders were filtrated, washed, and dried at 80 °C for 8 h in a vacuum oven.

2.2. Physicochemical characterization

X-ray diffraction patterns of mesoporous samples were collected on a PAN analytical X'Pert Pro diffractometer using Cu K α ($\lambda = 0.1542$ nm). The diffractograms were recorded in the 2θ range of 0.5–70° with a 2θ step size of 0.02 Å and a step time of 0.60 s. Nitrogen adsorption–desorption isotherms were measured at –196 °C on a NOVA 3200 Unit, USA apparatus. Samples were outgassed at 300 °C for 4 h prior to the nitrogen adsorption measurements. The specific surface area was calculated using the Brunauer–Emmett–Teller (BET) method. The pore size was obtained from the adsorption branch of the nitrogen isotherms. The morphology of the prepared samples was observed on a Quanta 250 FEG field emission scanning electron microscope (HR-FESEM) using an accelerating voltage of 30 kV equipped with EDAX EDS and GIF (Gatan Image Filter). Raman spectra were recorded with an HR-UV 800 confocal scanning spectrometer (Horiba Jobin Yvon), equipped with a microscope and a 514.5 nm Ar⁺ ion laser as the excitation source in the range of 400–2000 cm^{–1}. Thermogravimetric analyses (TGA & DSC) were performed using a SDTQ-600 (TA-USA) thermo balance instrument. The experiment was performed at 10 °C min^{–1} from room temperature to 800 °C in nitrogen at a flow rate of 100 mL min^{–1}. Pt dispersion was evaluated by H₂ pulse chemisorption at 25 °C on Chembet 3000 apparatus (Quantachrome, USA), through pulse titration equipped with a TCD detector. Prior to the pulse chemisorption experiments, all the samples were reduced under H₂/Ar flow (50 cm³ min^{–1}) for 1 h at 350 °C. For each pulse chemisorption analysis, about 40–50 mg of the sample was treated with an Ar flow of 50 cm³ min^{–1} and pulses of 0.05 cm³ (10% H₂ in Ar) until saturation of the catalysts. To calculate the metal dispersion, an adsorption stoichiometry of H/Pt = 1 was assumed.²² Dynamic light scattering (DLS) was performed to determine the particle size distribution of samples using a zeta-sizer nano series HT (Nano-ZS) (Malvern Instruments). To prepare the DLS samples, a dilute particle–tetrahydrofuran (THF) colloidal mixture was ultrasonicated for 30 min. The measurement was repeated at least 3 times for each sample to ensure the reproducibility. The temperature programmed desorption of ammonia (NH₃-TPD) was carried out to characterize the acid properties of the solid catalysts, providing information on the acid density and acid strength distribution using a dynamic chemisorption analyzer (B1 Cat II). Prior to NH₃ adsorption at 200 °C for 0.5 h, the sample was pretreated in a helium flow at 550 °C for 0.5 h. After that, the physically adsorbed NH₃ was removed in a flow of helium for 0.5 h, followed by heating to

700 °C at a rate of 10 K min^{–1}. The ammonia desorption signals were recorded with a TCD detector.

Catalytic activity. The catalytic activity of the prepared Pt nanoparticles-supported P-, O-, and N-OMCs was probed in *n*-heptane hydroconversion. The catalytic experiments were carried out in a fixed-bed continuous down-flow reactor operated under atmospheric pressure. Approximately 0.1 g of the catalyst was loaded into the quartz tube and pretreated under a H₂ flow at 450 °C for 2 h. The *n*-heptane was fed into the reactor using a syringe pump. The reaction conditions used in this work were: a H₂ flow of 1.8 L h^{–1}, molar ratio of H₂/*n*-C₇ of 14, and space velocity of 1.5 h^{–1}. The conversion was changed by varying the reaction temperature from 300 °C to 500 °C. The liquid products were analyzed on-line with a gas chromatograph (Agilent Technologies-7890A) equipped with a flame ionization detector and a capillary column (HP-30m).

3. Results and discussion

3.1. Structural and morphological characterization of the SBA-15 template, P-OMC, O-OMC, and N-OMC supports

Different analytical and spectroscopic techniques were used to study the physicochemical characteristics of the template SBA-15 and the P-OMC, O-OMC, and N-OMC samples.

The small-angle XRD (SAXRD) diffraction patterns were recorded to check the structural ordering of the parent SBA-15 employed as the hard template for the preparation of P-OMC and N-OMC (Fig. 1). Well-resolved XRD peaks could clearly be observed at $2\theta = 0.9^\circ$, 1.5° , and 2.4° , which correspond to the (100), (110), and (200) diffractions of 2D hexagonal mesostructure, corresponding to the hexagonal *P6mm* symmetry, indicative of the good quality of the template sample. The P-OMC and

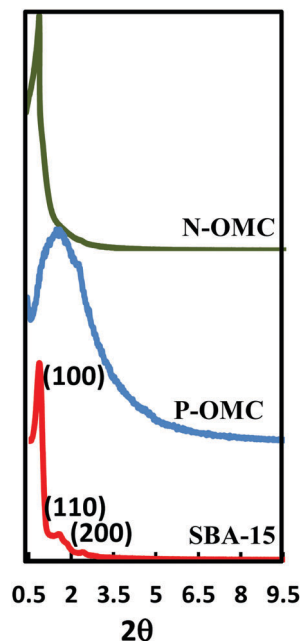


Fig. 1 SAXRD patterns of SBA-15, P-OMC, and N-OMC.

N-OMC samples replicated from the SBA-15 template also showed (100) diffraction peak at a relatively higher 2θ of 2.7° and 1.3° , respectively, and less resolved higher order (110) and (200) (*i.e.*, decreased unit cell dimension), indicating that the ordered mesoporous structure with a two-dimensional (2D) hexagonal symmetry of the template was replicated into the carbon samples with a little structural shrinkage or deterioration.²³ A notable decrease in the intensity of the (100) diffraction peak of the P-OMC replicated sample was observed, indicating that the high-temperature carbonization indeed had a substantial influence on the self-assembly process causing shrinkage of the carbon frameworks leading to the lack of long-range structural ordering.²⁴

Wide-angle XRD (WAXRD) and Raman spectroscopy were carried out to study the graphitization and the prepared samples orderliness degree (Fig. 2A and B). As shown in (Fig. 2A), the WAXRD of the SBA-15 hard template exhibited one broad hump at $2\theta = 20^\circ$ due to amorphous silica. After nanocasting the (P-OMC), oxidation (O-OMC), and nitrogen-doping (N-OMC) samples, a broad peak at 21° and a slight one at 43° corresponding to graphite (002) and (101) planes of graphite were observed. These peaks are characteristic of the partially graphitic wall structure, which confirmed the presence of small amounts of stacked crystalline graphite phase.²⁵ From the XRD results, we assumed that the pristine OMC and N-OMC structures were reverse replicas of SBA-15. This indicates that the ordered mesostructure was maintained even after the nanocasting process and thermal treatment at 900°C . Upon modification of the P-OMC sample surface by acid oxidation ($\text{K}_2\text{S}_2\text{O}_8/\text{H}_2\text{SO}_4$), a higher graphitization degree was attained, which could be distinguished by the increased intensity of the (100) plane at 43° compared with the P-OMC and N-OMC samples. In the Raman spectra (Fig. 2B), two prominent peaks can be observed: one at 1321 cm^{-1} , related to the vibration of carbon atoms of disordered graphite (D band) and another at 1578 cm^{-1} attributed to the vibration of sp^2 -bonded carbon atoms in the 2D hexagonal lattice (G band).²⁶ The intensity of the 1321 cm^{-1} line increases with the increase in carbon content within the samples and with the decrease in the graphite crystal size. The relative intensity of the D and G bands ($I_{\text{D}}/I_{\text{G}}$) is an indicator of the degree of in-plane defects crystalline dimensions and edge

defects in the carbon materials and hence depends on the graphitization degree.^{26,27} Commercial graphite exhibits an $I_{\text{D}}/I_{\text{G}}$ value of 0.366.²⁸ The $I_{\text{D}}/I_{\text{G}}$ ratio of P-OMC (1.14) was higher than that of O-OMC (0.98) and N-OMC (1.04) and also much higher than that of pure graphite, indicating that these OMCs samples were not very well crystallized and had a low graphitization degree.²⁹ The observation of the low graphitic structures was consistent with the wide-angle XRD results (Fig. 2A). It is well known that using sucrose as a hydrocarbon precursor leads to the formation of a non-graphitic carbon structure after pyrolysis. Also, comparing the $I_{\text{D}}/I_{\text{G}}$ values among the three samples, it could be suggested that the surface modification by oxidation generates tiny graphitic domains with edges serving as defects,³⁰ indicating that the graphitization degree of O-OMC outweighs than that of both the P-OMC and N-OMC samples.

The change of morphology and the average particle size during carbon replication were examined using FE-SEM images and the micrographs are presented in Fig. 3. The SEM image of the SBA-15 silica hard template shows a highly ordered array of a regular and uniform longitudinally arranged rod-like morphology corresponding to the $P6mm$ structure.³¹ The typical hexagonal rod-like structure of SBA-15 was also manifested on the SEM for all the carbon samples and exhibited well-organized pores parallel to one another, confirming the good replication process. The ordered rod-like morphology of all the carbon samples proved to be slightly damaged. However, the SEM image of the O-OMC sample was composed of small shaped rod-like particles that were agglomerated together, indicating severe structural damage caused by oxidation of the P-OMC surface by using the strong acids.

To verify the FE-SEM results, dynamic light scattering (DLS) measurements were carried out. The average particle size measurements are given in Table 1. As the mesoporous carbons are hydrophobic in nature the aggregation of particles took place easily in the polar solvent THF which was used to disperse the samples. The morphologies and dimensions of OMC were relatively homogeneous. The DLS results revealed that the particle sizes of P-OMC, N-OMC, and O-OMC were ~ 136 , 239 , and 807 nm , respectively (with a sharp distribution), which were all greater than that of SBA-15 (77 nm).

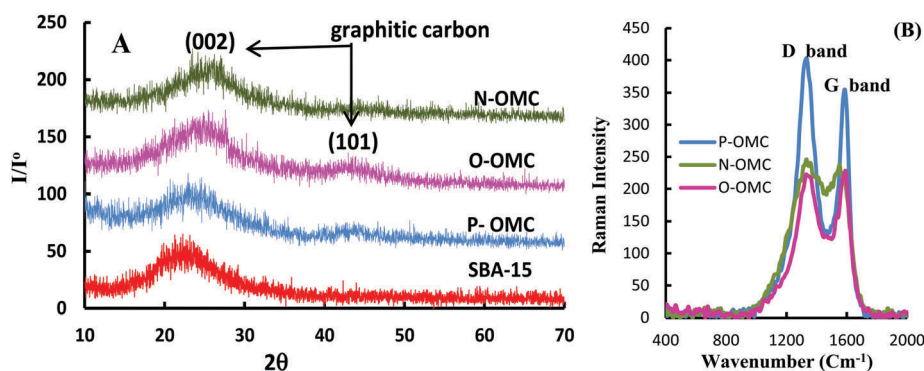


Fig. 2 (A) Wide-angle XRD patterns and (B) Raman spectra of the prepared samples.

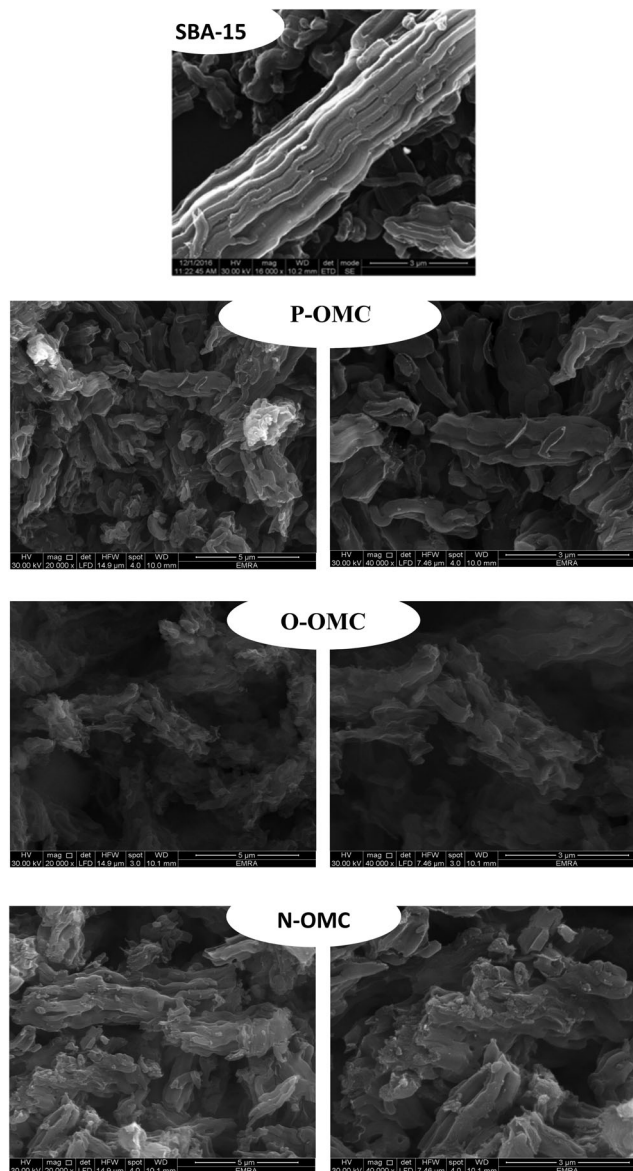


Fig. 3 FE-SEM images of the SBA-15 hard template and the prepared OMC samples.

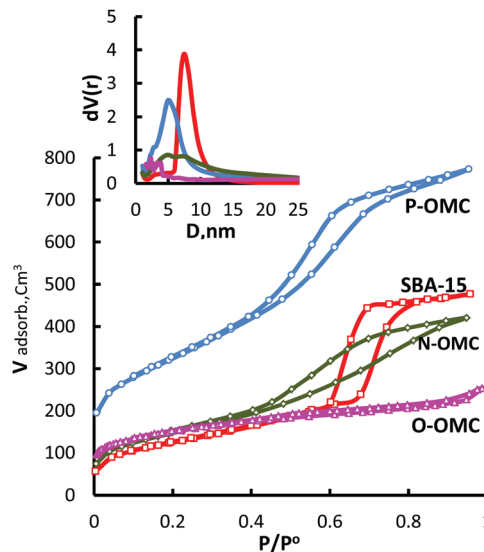


Fig. 4 N_2 adsorption/desorption isotherms of SBA-15, P-OMC, O-OMC, and N-OMC supports.

The porosity changes of the SBA-15 hard template, P-OMC, O-OMC, and N-OMC were obtained from nitrogen adsorption/desorption isotherms (Fig. 4), and the corresponding pore size distribution curves were calculated from adsorption branch of the isotherms by the BJH method (Fig. 4, inset). Also their textural parameters are listed in Table 1. SBA-15 shows characteristic a type IV adsorption/desorption isotherm with an H1-type hysteresis loop, indicating capillary condensation inside the uniform 2D cylindrical pores, which is a sure indicator of the mesoporous nature of the hard template material.³² The narrow H1 type hysteresis loop also indicated a high degree of pore-size uniformity of SBA-15, as shown in the pore size distribution of SBA-15 (Fig. 4, inset) with a sharp peak at 7.5 nm, indicating a quite regular array of mesopores. The P-OMC and N-OMC samples exhibited a type IV isotherm, confirming the successful replication of mesoporosity from the silica template (SBA-15) onto the P-OMC and N-OMC. However, they possessed a hysteresis loop of the H₂ type located at a smaller relative pressure range ($p/p^0 \sim 0.4$), suggesting the

Table 1 The structural textural parameters of the OMCs and Pt NPs-loaded OMCs samples

Sample	Average particle size ^a	Surface area results						
	nm	S_{BET}^b ($\text{m}^2 \text{g}^{-1}$)	S_{micro}^e ($\text{m}^2 \text{g}^{-1}$)	S_{ext}^e ($\text{m}^2 \text{g}^{-1}$)	V_{micro}^e (cc g^{-1})	V_{meso}^f (cc g^{-1})	TV_p^c (cc g^{-1})	D_p^d (nm)
SBA-15	77	450	0	450	0	0.74	0.74	7.5
P-OMC	136.2	1144	354	790	0.19	1.01	1.2	4.40
10% Pt/P-OMC(EG)	522.1	925	266	659	0.12	1.08	1.2	3.30
N-OMC	238.5	531	74	457	0.04	0.62	0.66	3.85
10% Pt/NOMC(EG)	141.8	533	164	369	0.07	0.55	0.62	3.71
O-OMC	806.7	512	356	156	0.15	0.24	0.39	1.62
10% Pt/O-OMC(EG)	462.1	543	401	142	0.16	0.25	0.41	1.64

^a By DLS. ^b Total surface area calculated by BET method. ^c The total pore volumes were estimated at $P/P^0 = 0.98$. ^d The mean pore size diameter of the samples calculated from the BJH method. ^e The micropore surface area (S_{micro}), external surface area (S_{ext}), and micropore volume (V_{micro}) of the samples were determined using t -plot analysis. ^f The mesopore volumes (V_{meso}) were calculated by subtracting the micropore volume (V_{micro}) from the total pore volume.

existence of disordered pores and a smaller pore size (FE-SEM images, Fig. 3). The only exception was the nitrogen adsorption curve of the O-OMC sample with much lower N_2 -adsorbed amounts and a broad featureless hysteresis loop, which means that a large number of micropores were blocked and/or damaged during the acid oxidation treatment of the P-OMC surface. It is hypothesized that the oxidation of the surface carbon species happens at the micropore/small mesopore openings as a priority. As a result the oxygen-containing groups attached to the pore openings can probably block the micropores leading to a severe reduction of the measured pore surface area and volume.³³ Using the Brunauer–Emmett–Teller (BET) equation, the surface area and pore volume of SBA-15 and the OMCs were determined and the results are presented in Table 1. It should be noted that the carbon replica P-OMC sample exhibited a high BET specific surface area ($S_{\text{BET}} = 1144 \text{ m}^2 \text{ g}^{-1}$) and total pore volume ($TV_{\text{p}} = 1.2 \text{ cc g}^{-1}$), which is consistent with the N_2 isotherm curve. These parameters are comparable with those published previously for OMC materials.^{34,35} Its porosity constituted of both micropores ($V_{\text{micro}} = 0.19 \text{ cc g}^{-1}$), which may be formed due to the high carbonization temperature ($900 \text{ }^\circ\text{C}$), and mesopores replicated from the SBA-15 template ($V_{\text{meso}} = 1.01 \text{ cc g}^{-1}$). After the modification of the P-OMC surface with KPS and $\text{H}_2\text{S}_2\text{O}_4$ treatment, the BET specific surface area and the total pore volume values diminished from 1144 to $512 \text{ m}^2 \text{ g}^{-1}$ and from 1.2 to 0.39 cc g^{-1} , respectively (Table 1), suggesting that the oxidation treatment caused severe changes in the morphology and consequently in the porosity. However, compared to the template SBA-15 sample, the decreased pore volume and average pore diameter of N-OMC sample indicated the successful incorporation of the N-containing organic moieties onto the pore surface of the mesostructure.

The surface composition of SBA-15, and the P-OMC, O-OMC, and N-OMC samples was analyzed by their FT-IR spectra (Fig. 5). The FT-IR results demonstrated a significant difference among the FT-IR spectra obtained for the prepared samples. There are two typical peaks that characterize the Si-O_x stretching range for SBA-15 as follows: $\nu_{\text{OH}}(\text{H}_2\text{O})$ 3380 cm^{-1} , $\delta \text{OH}(\text{H}_2\text{O})$ 1618 cm^{-1} , which could be assigned to isolated silanol groups and adsorbed water on the surface of the solid. Additionally, three bands are related to intrinsic vibrations, symmetric $\nu_{\text{s}}(\text{Si-O-Si})$ and asymmetric $\nu_{\text{as}}(\text{Si-O-Si})$, of the

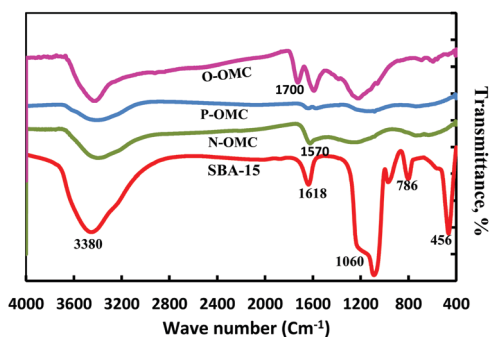


Fig. 5 FT-IR spectra of the prepared OMCs.

tetrahedral unit SiO_4^{4-} (at 786 and 1060 cm^{-1} , respectively) and the other one is assigned to the stretching vibration, $\delta\text{OH}(\text{Si-OH})$, of Si-O moiety of the silanol groups $\text{Si-O}\cdot\cdot\text{H}$ on the surface at 938 cm^{-1} . One additional peak was evident at the low wave number corresponds to the same tetrahedral unit SiO_4^{4-} , $\delta(\text{Si-O-Si})$ at 461 cm^{-1} .³⁶ On the other hand, The FT-IR spectra of the P-OMC sample (Fig. 5) revealed the absence of the bands associated with Si-O-Si at 1060 , 938 and 786 & 461 cm^{-1} , indicating that the samples were free from the mesoporous silica template confirming that the structure of the OMC prepared sample came from the carbon and not from the template, with the weak bands at around 1600 and 1550 cm^{-1} were characteristic for carbon materials.³⁷ Also, the very broad band located at 3380 cm^{-1} became mild indicating fewer amounts of OH groups. The pristine mesoporous carbon was dominantly composed of carbon ($\sim 92 \text{ wt}\%$) with only a small amount of H and O. Upon oxidation of the pristine OMC surface, several new bands appeared. First a new intense band at 1700 cm^{-1} was assigned to the C=O stretching vibrations in lactone, carboxylic anhydride, and/or carboxylic acid,³⁸ indicating the generation of a high density of carboxylic groups. Second, a new band at 1169 cm^{-1} was attributed to the C-O stretching vibrations in ether, lactone, phenol, and/or carboxylic anhydride,³⁹ implying the generation of many surface oxides. The strong band at 1561 cm^{-1} could be ascribed to symmetric COO^- vibration and/or the C-C stretching vibrations in an aromatic ring coupled to highly conjugated keto-enol groups.⁴⁰ In addition, the absence of the characteristically sharp band near 670 cm^{-1} ascribed to $\text{S}_2\text{O}_8^{2-}$ confirmed that the $\text{S}_2\text{O}_8^{2-}$ ions had been thoroughly washed away. Finally, the band centered at about 3374 cm^{-1} became more pronounced, probably due to the contribution by the $-\text{COOH}$ groups generated. The FT-IR spectra of the N-OMC (Fig. 5) showed no peak associated with Si, revealing that the mesostructure was generated from the true replication process and the silica framework removal process using HF was highly efficient and successful. Also, a peak was observed at 1570 cm^{-1} corresponding to the C=N bond.⁴¹

Fig. 6 demonstrates that there was no significant difference among the TGA–DSC profiles obtained from SBA-15, and the N-OMC, pristine OMC, and O-OMC samples. As shown in Fig. 6, all the samples exhibit a small weight loss event below $100 \text{ }^\circ\text{C}$, corresponding to the removal of adsorbed water associated with a DSC endothermic peak centered at around $160 \text{ }^\circ\text{C}$. The TG profile (Fig. 6) shows that the pristine OMC had a weight loss, with $\sim 13 \text{ wt}\%$ in total up to $600 \text{ }^\circ\text{C}$. However, after oxidation of the P-OMC surface, the O-OMC sample showed a considerable weight loss (Fig. 6). Three main weight loss stages could be observed. The first one at $30\text{--}150 \text{ }^\circ\text{C}$ lost $11 \text{ wt}\%$, which was attributed to the dehydration of physisorbed water. At $150\text{--}350 \text{ }^\circ\text{C}$ a second weight loss of $\sim 14\%$ was observed which probably was related to the decomposition of the functional carboxylic and phenolic groups.⁴² The weight loss below $280 \text{ }^\circ\text{C}$ was ascribed to the decomposition of carboxylic groups, while those from $280\text{--}350 \text{ }^\circ\text{C}$ were ascribed to the phenolic groups, since the carboxylic groups can decompose at a lower temperature than phenolic groups.⁴³ The third stage with

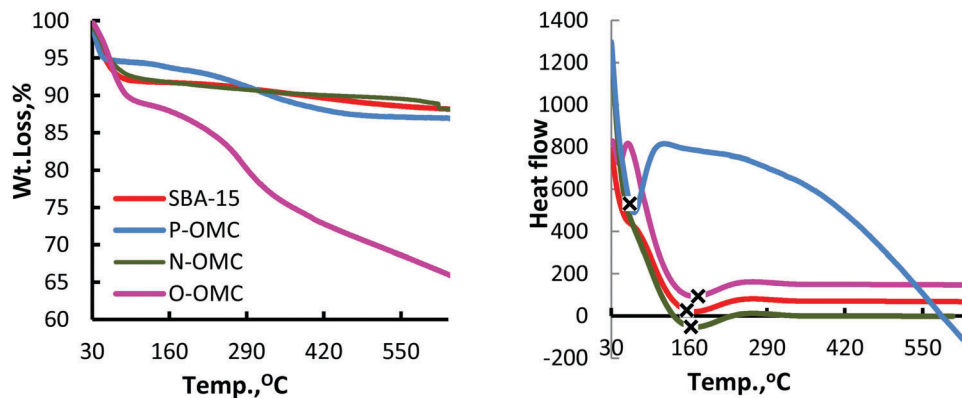


Fig. 6 TGA and DSC profiles of SBA-15 and the OMC prepared samples.

another 10 wt% weight loss occurred from 350–600 °C, which could be attributed to the decomposition of lactone, quinone, and anhydride groups.⁴⁴ The high density of surface oxides of O-OMC was further confirmed by the TGA profile. From the TGA results, the functionalization of the OMC surface increased the hydrophilicity of the modified carbon samples showing a high affinity toward water adsorption because of the high content of functional groups on the surface.

3.2. Characterization of Pt NPs-supported P-, O-, and N-OMC catalysts

The high surface area of OMC can provide more surface anchoring sites or functional groups for the nucleation of metal nanoparticles compared with conventional carbon blacks, such as Vulcan XC-72R and Ketjen Black, and allows the preparation of metals-supported OMCs with a high dispersion degree. Also, the uniform mesoporous structure of OMC facilitates the diffusion of reactive molecules for hydroconversion reactions. In the present work, P-, N-, and O-OMCs were efficiently used as supports for the preparation of Pt NPs bifunctional catalysts by using ethylene glycol as a reduction agent without any surfactant or hydrothermal process. The total loading of Pt was controlled to be as high as 10 wt%. A series of characterization methods were performed to confirm the successful loading of 10 wt% Pt/OMCs onto various OMCs samples and to investigate their physicochemical characterizations.

In the large-angle region of the XRD patterns (Fig. 7), all the Pt-supported P-, O-, and N-OMC samples showed a characteristic diffraction peak at $2\theta = 39.8^\circ$ and less resolved two peaks at around 46.2° , and 67.8° assigned to the (111), (200), and (220) planes, respectively, revealing the presence of Pt metal (Pt(0)) NPs with a face-centered cubic (fcc) crystal phase structure, indicating the effectiveness of Pt deposition to its metal state by the EG reduction method. In addition, a broad diffraction peak at 25° was also observed corresponding to the graphite(002) plane of OMCs.

The morphology and metal dispersion of Pt NPs were further verified by FE-SEM measurements and the results are presented in Fig. 8. The SEM image of the Pt/P-OMC sample had a distinguishable morphology change compared with the P-OMC

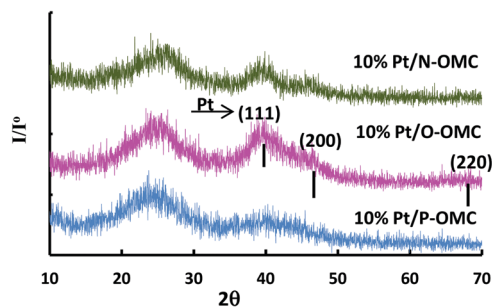


Fig. 7 XRD patterns of the Pt NPs-supported various OMCs.

support and exhibited a higher density of platinum particles with an even distinguished agglomeration, which led us to postulate the formation of large particle Pt clusters with high dimensions; in contrast, the bright-field SEM images observed for the Pt/O-OMC and Pt/N-OMC samples indicated an ordered array of mesoporous carbon nanorods ideally decorated with Pt nanoparticles, revealing that the surface modification either by oxidation and/or nitrogen-doping were helpful for stabilizing the Pt NPs on the surface of OMC rods, which provoked not only a higher dispersion of Pt NPs on the functionalized carbon surface but also an ordered structure, which could lead to the higher accessibility of these Pt nanoparticles toward reactants.

As described in Table 2, full energy dispersive X-ray spectroscopy (EDX) attached with FE-SEM instrument analysis showed different wt% for all the Pt-supported OMCs, although all had the same Pt loading of *ca.* 10 wt%. However, the Pt/P-OMC samples possessed a low Pt. content (8.85 wt%). This may be due to the weak interaction between Pt nanoparticles and the non-functionalized surface of the P-OMC sample; consequently, the Pt nanoparticles tended to aggregate on the external surface area of P-OMC and form large Pt clusters (see SEM image, Fig. 8 with a magnification of 5 μm)—this was in accordance with the drop in the external surface area value from 790 to 640, the increase of the average particle size from ~ 136 to 522 (Table 1), and constituent with the Pt average particle sizes (57 nm) as estimated by H_2 -chemisorption analysis (Table 2) causing the low dispersion (20%) for the Pt NPs metal displayed in the EDX

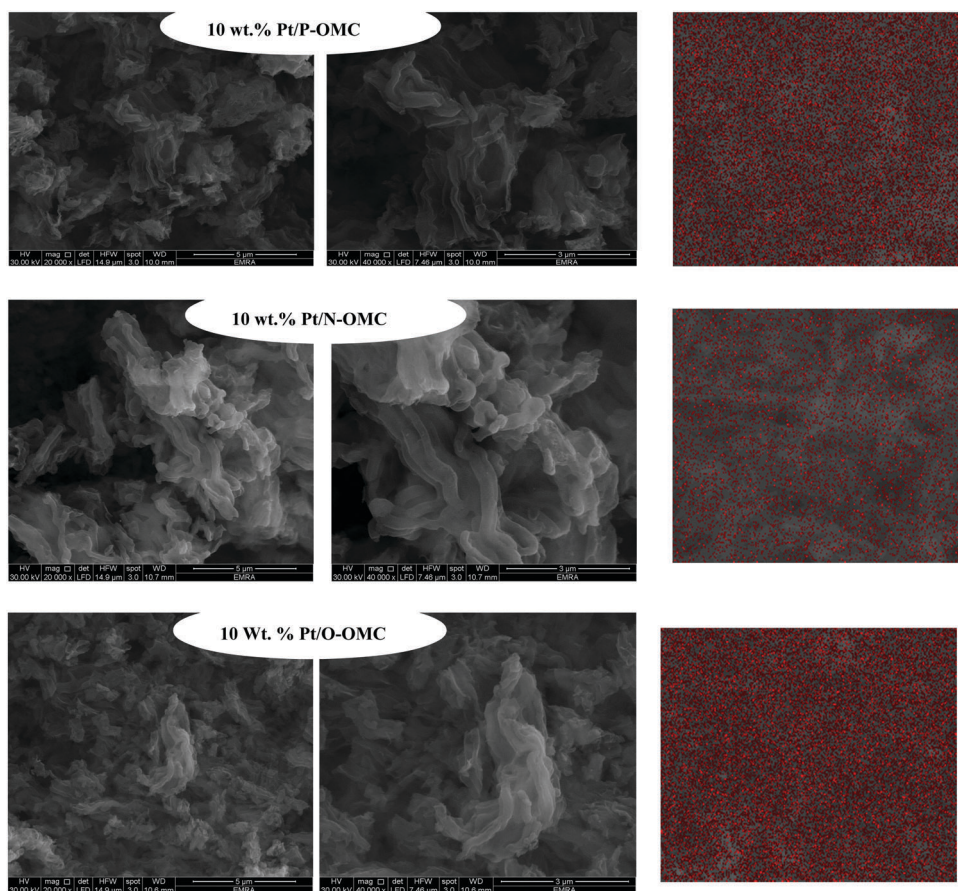


Fig. 8 FE-SEM (left) and Pt EDX mapping images (right) of the Pt NPs-supported various OMCs.

Table 2 Physical Properties of Pt-loaded OMCs samples

Sample	Characterization of metal function				Acidity ^e ($\mu\text{mol g}^{-1}$)			
	Pt ^a (wt%)	D^b (%)	S_{Pt}^c ($\text{m}^2 \text{g}^{-1}$)	d_{Pt}^d (nm)	Weak	Medium	Strong	Total
10% Pt/P-OMC(EG)	8.85	20.02	4.38	56.56	—	0.284	—	0.248
10% Pt/N-OMC(EG)	9.38	44.79	10.38	25.28	0.117	0.074	0.251	0.442
10% Pt/O-OMC(EG)	9.97	27.54	6.78	41.13	0.053	0.181	0.398	0.632

^a Pt concentration determined by EDX. ^b Dispersion by H_2 pulse chemisorption. ^c Platinum surface area by H_2 pulse chemisorption. ^d Average Pt particle size by H_2 pulse chemisorption. ^e By NH_3 -TPD.

image mapping of the Pt element in Fig. 8. These results are constituent with the drops in the S_{BET} , TV_p , and D_p values of the P-OMC support upon Pt loading (Table 1). As expected, in comparison with Pt/P-OMC, Pt/O-OMC and Pt/N-OMC EXD analysis showed a relatively high Pt. content (9.97 wt% and 9.38 wt%, respectively), close to the real loaded amount, which could be inferred that the surface modifications by heteroatoms incorporation (either N and/or O) into carbon materials led to enhanced π bonding and acted as anchoring sites for the metallic Pt NPs,⁴⁵ and hence Pt was more homogeneously distributed in both the N-OMC and O-OMC matrix supports. The average platinum particle size obtained by H_2 -chemisorption decreased from 57 nm on P-OMC to 41 and 25 nm on O-OMC and N-OMC, respectively, facilitating the high dispersion of Pt nanoparticles with 45% and 28% (Fig. 8 and Table 2) and causing

the shrinkage of the average particle size to half compared to the non-Pt-loaded samples (Table 1). Also, the aforementioned results can justify the increase in textural parameters of the platinum-supported N-OMC and O-OMC samples (Table 1) and were in good agreement with the FE-SEM images.

Meanwhile, the N_2 adsorption/desorption isotherms of Pt-loaded OMCs samples exhibited similar shapes with those of OMC supports of type IV with well-defined H_2 hysteresis loops, except for the decreased adsorption N_2 quantity. Furthermore, it is interesting to point out that the pore size distribution curves (Fig. S1, ESI[†]) obtained using the BJH method revealed that there was no displacement of the maximum position. This suggests that shrinkage of the average pore sizes was motivated by a partial pore plugging rather than pore blocking upon immobilization of the Pt NPs.

More abundant defect sites on Pt/N-OMC with $I_D/I_G = 0.99$ was confirmed by the Raman spectra (Fig. S2, ESI†) results, allowing facile nucleation of Pt nanoparticles and leading to a higher Pt loading,⁴⁶ matching the results estimated by H₂-chemisorption. While $I_D/I_G = 0.83$ and 0.85 for the Pt/O-OMC and Pt/P-OMC samples, respectively, indicating the graphitization degrees of the P-OMC and N-OMC increased upon loading Pt NPs.

Fig. S3 in the ESI† presents TG curves of the Pt NPs-supported samples in a nitrogen atmosphere, in the temperature range of 30–800 °C. The TGA plots demonstrate the similarity for all the Pt-supported various OMCs samples, differing only in the temperatures where the thermal event occurs. The TGA isotherms showed only one thermal event at ~140 °C due to dehydration of the physisorbed water with a total weight loss of ~43%, 20%, and 9% for the Pt/P-OMC, Pt/O-OMC, and Pt/N-OMC samples, respectively. From the TGA curve, it can be concluded that the Pt supported various OMCs to have a thermal stability up to 600 °C.

The relationship between the acid sites density of the Pt NPs-supported P-, O-, and N-OMC catalysts and their catalytic activities were clarified by studying their NH₃ adsorption/desorption behaviors, and the results are shown in Fig. 9 and summarized in Table 2.

TGA curves (Fig. S3, ESI†) show that the high content of physisorbed water was removed at 100 °C in the presence of N₂ and the weight of the samples then kept steady. Thus the adsorption of NH₃ was conducted at 110 °C to highlight the adsorption by the weak acid sites by eliminating the weak physisorption. As shown in Fig. 9, the TPD-NH₃ profile for Pt NPs-supported P-OMC exhibited one sharp peak at ca. 352 °C, ascribed to medium-strength acid sites. Meanwhile, the TPD-NH₃ profiles for the Pt NPs-supported N-OMC and O-OMC catalysts showed three acid sites of different strengths depending on the temperature that ammonia desorption takes place. Below 200 °C is assigned to the weak acid sites peak, while peak after 390 °C is due to strong acid sites, and the intermediate peak is caused by medium acid sites. Overall, the total acid sites density increases according to the following order: 10% Pt NPs/O-OMC ($0.632 \mu\text{mol-NH}_3 \text{ g}^{-1}$) > 10% Pt NPs/N-OMC ($0.442 \mu\text{mol-NH}_3 \text{ g}^{-1}$) > 10% Pt NPs/P-OMC ($0.284 \mu\text{mol-NH}_3 \text{ g}^{-1}$), suggesting the positive effect of OMC surface modification either by oxidation and/or by nitrogen-doping, improving the acidity of the Pt NPs-supported catalysts, since the catalyst acidity is determined mainly by the support.

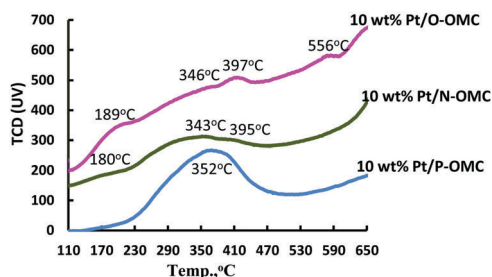


Fig. 9 NH₃-TPD profiles of Pt NPs supported various OMCs.

Table 2 demonstrates that the 10% Pt NPs/P-OMC and 10% Pt NPs/O-OMC catalysts had the highest content of medium acid site densities with $0.284 \mu\text{mol-NH}_3 \text{ g}^{-1}$ and $0.181 \mu\text{mol-NH}_3 \text{ g}^{-1}$, respectively, while an opposite sequence was presented in terms of strong acid sites, where the greatest value was for the 10% Pt NPs/O-OMC catalyst with $0.398 \mu\text{mol-NH}_3 \text{ g}^{-1}$ then the 10% Pt NPs/N-OMC catalyst with $0.251 \mu\text{mol-NH}_3 \text{ g}^{-1}$. Furthermore, the 10% Pt NPs/N-OMC catalyst exhibited more weak acid sites compared to the 10% Pt NPs/O-OMC catalyst. A shift of the strong acid sites NH₃ desorption peak from 395 °C on 10% Pt NPs/N-OMC catalyst to 397 °C and 556 °C, indicating a major increase in the acid site strength for 10% Pt NPs/O-OMC catalyst. It is proposed that weak-strength acid sites favor the skeleton isomerization reaction, while strong acid sites ones enhance the possibility of the cracking.

4. Hydroconversion of *n*-heptane

4.1. Effect of surface modification of the OMC support on the hydroconversion reaction of *n*-heptane

The effect evolution of the functionalization of ordered mesoporous carbon surface used as a support on the catalytic performance of the bifunctional Pt NPs-supported P-OMC, N-OMC, and O-OMC catalysts was investigated toward *n*-C₇ hydroconversion using a fixed-bed reactor operated under atmospheric pressure at a reaction temperature range of 300–500 °C, and the results are illustrated in Fig. 10–13. The results cover *n*-C₇ hydroconversion, converted product distributions and the selectivity. The major converted products were composed of: (1) *i*-C₇ isomers, (2) methyl cyclohexane, and (3) toluene.

As shown in Fig. 10, the three studied catalysts followed the common behavior trend; where conversion increased with raising the reaction temperature, regardless of the nature of the carbon support or the dispersion of the Pt NPs degree. Overall the three studied catalysts exhibited low catalytic activity with *n*-C₇ conversion: ~7% at a reaction temperature below 350 °C. Nevertheless, the *n*-C₇ total conversion increase rapidly with the temperature afterwards for the Pt NPs-supported P-OMC and O-OMC catalysts. Both catalysts exhibited a highest *n*-C₇

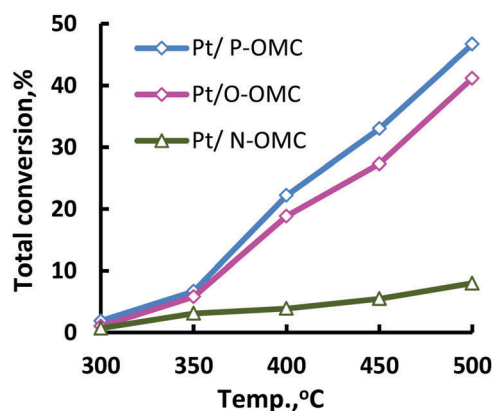


Fig. 10 Conversion of *n*-heptane as a function of the reaction temperature over Pt NPs-supported P-, O-, and N-OMC catalysts.

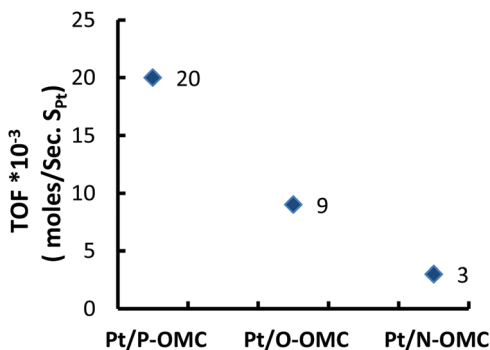


Fig. 11 Effect of different Pt NPs dispersion degrees of the supported P-, N-, O-OMC catalysts on the TOF of *n*-heptane at reaction temperature of 350 °C.

conversion of above 40% at the reaction temperature of 500 °C. While, the Pt NPs-supported N-OMC catalyst showed extremely low catalytic activity as the *n*-C₇ conversion of monotonic increased with the reaction temperature, reaching 8% total conversion at 500 °C.

It is generally recognized that when paraffin hydroconversion is performed over solid supported noble metal bifunctional catalysts, an adequate ratio between the metal sites and the surface acid sites of the support surface is critical to obtain high catalytic performance.⁴⁷ The differences in the catalytic performance of the three catalysts toward *n*-heptane hydroconversion were consistent with the characterization results of the Pt metal dispersion degree and the acidity strength. The catalytic performance over the Pt/P-, O-, and N-OMC bifunctional catalysts correlated positively with the medium-strength acid density on the catalyst surface in the order of P-OMC > O-OMC > N-OMC (Table 2), which was required to provide easier activation for *n*-C₇ conversion. In general, it is necessary for the supported catalysts to hold sufficient acid sites with considerable acid strength for achieving high catalytic activity, which clarified the relatively low catalytic activity of Pt/N-OMC compared with the Pt NPs-supported P-OMC and O-OMC catalysts. The sequence of the catalytic activity performances of the prepared catalysts as a function of the medium acid site strength values varied according to the following order: Pt/P-OMC (46%) > Pt/O-OMC (41%) > Pt/N-OMC (8%).

To investigate the effect of different Pt dispersion degrees on the different catalytic performances of the prepared Pt/P-, N-,

and O-OMC catalysts, the turnover frequency (TOF) was thus calculated. The TOF is defined as the no. of moles of *n*-heptane converted/platinum metal site surface area estimated from the dispersion degrees, which are directly related to the average size of the Pt NPs (Table 2)/second. The TOF calculated values for *n*-heptane conversion as a function of the different modified catalyst support OMC surfaces are shown in Fig. 11. It was clearly observed that *n*-heptane at 350 °C had very different TOF numbers depending on the dispersion degree of the Pt NPs. Fig. 11 illustrates that *n*-heptane hydroconversion increased with the decrease in the dispersion degree of Pt NPs metal supported on different catalyst supports, similar to the conversion trend in Fig. 10. Thus one can assert that the superior catalytic performance of the Pt/P-&O-OMC catalysts compared with that of Pt/N-OMC mainly originated from the improved medium acid sites on the P-, and O-OMC catalyst support, which is favorable for maintaining the well-presented synergistic interaction between the Pt NPs metallic clusters and acid sites.

The Pt NPs-supported P-OMC, O-OMC, and N-OMC catalysts showed qualitatively similar types of *n*-C₇ converted products, including: (a) isoheptanes, (b) cyclization products (methylcyclohexane), (c) aromatic products (toluene), and (d) trace amounts of cracked products (light hydrocarbons) that appeared only at 500 °C (Fig. 12). This may be owing to the mesoporous character of the OMC supports that promotes the occurrence of more than one reaction on the acid sites before reaching the hydrogenating sites; thus allowing the formation of bulky molecules. The cyclization of *n*-C₇ into methyl cyclohexane occurred at a low reaction temperature (at the beginning of reaction), *i.e.*, it is a primary product. Its yield trended upward to a maximum with 8.2%, 5.7%, and 1.4% at 400 °C over the Pt NPs-supported P-OMC, O-OMC, and N-OMC catalysts, respectively, and then decreased with the temperature in parallel with the increase in the aromatic product. The behavior of the isomerization reaction (*i*-C₇ production) followed the same pattern of methylcyclohexane, *i.e.*, *i*-C₇ yield formation depends on the reaction temperature. They passed through a maximum at 350 °C, as clearly shown in Fig. 12, and then decreased with the reaction temperature due to the thermodynamic limitation and the higher activation energy for the isomerization reactions.⁴⁸ This maximum was clearly observed for the Pt NPs-supported functionalized ordered mesoporous carbon surfaces (N-OMC and O-OMC) catalysts. In fact the methyl cyclohexane and *i*-C₇ yield

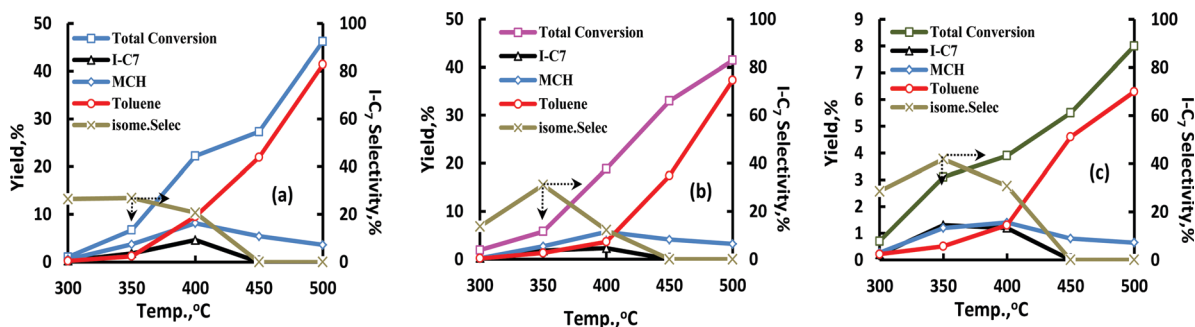


Fig. 12 Converted product distributions and *i*-C₇ isomers selectivity over: Pt NPs-supported (a) P-OMC (b) O-OMC, and (c) N-OMC catalysts.

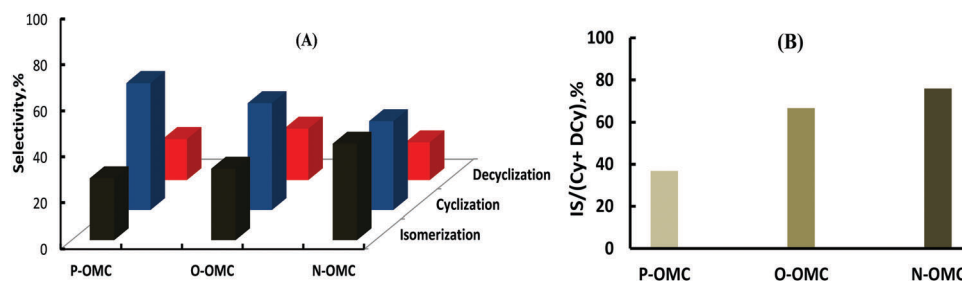


Fig. 13 (A) Selectivity of the different product distributions (B) ratio between isomerization and the sum of cyclization and dehydrocyclization (IS/(Cy + DCy)) over the three studied catalysts.

formation curves quickly reached a maximum and then fell to zero (suggesting that both products are very reactive intermediates). However, the aromatization reaction (toluene formation) was predominant at high reaction temperatures over all the studied catalysts (Fig. 12). The yield of toluene was as high as 41% and 37% at 500 °C over the Pt NPs-supported P-OMC and O-OMC catalysts, respectively, and then decreased to 6% at 500 °C upon using the Pt NPs-supported N-OMC catalyst.

Regardless of the carbons support, it could be observed that the isomerization and cyclization reaction of *n*-C₇ to *i*-C₇ and methyl cyclohexane were catalyzed at lower reaction temperatures (300–400 °C), while the dehydrocyclization reaction of *n*-C₇ into toluene was activated at higher reaction temperatures (400–500 °C). Changes in the activity due to isomerization, cyclization, and dehydrocyclization can be related to the effect of the OMC support functionality and hence the variation of the density, acid strength, and the Pt NPs metal dispersion. A poor Pt NPs metal dispersion and a moderate acidic strength are indicative of high methyl cyclohexane and toluene products formation, *i.e.*, cyclization and dehydrocyclization over the isomerization reaction for the Pt NPs-supported P-OMC and O-OMC catalysts. Whereas the Pt NPs-supported N-OMC bifunctional catalyst had an adequate balance between the weak acidic strength and Pt NPs metal sites dispersion that facilitated the occurrence of the isomerization reaction, resulting in the highest isomerization yield, which represents the most valuable products compared with cyclization and dehydrocyclization products yield formation.

The hydroconversion of *n*-C₇ was accompanied by a remarkably low isomer selectivity. The low selectivity toward *i*-C₇ at high reaction temperatures (> 350 °C) may be caused by the strong tendency of *i*-C₇ consumption in the formation of cyclization (methyl cyclohexane) and dehydrocyclization (toluene) products. The histogram in Fig. 13A represents the converted product distribution selectivity over the three studied catalysts at a reaction temperature of 350 °C. The three studied catalysts were able to form isomers, methylcyclohexane, and toluene products. It was clarified that the isomerization is the main reaction; with more than 40% selectivity over Pt NPs-supported N-OMC catalyst, but this decreases to about 30% and 26% over the Pt NPs-supported O-OMC and P-OMC catalysts, respectively. This is substantially consistent with the combination of the more weak-strength acid site density and the homogeneous dispersion of Pt NPs

metal (Table 2) achieved for the Pt NPs-supported N-OMC catalyst. The formation of methyl cyclohexane products due to the cyclization reaction of *n*-heptane with 55%, 47%, and 39% selectivity was obtained over the Pt NPs-supported P-OMC, O-OMC, and N-OMC catalysts matches the variations of medium-strength acid site density (mild acidity) over the three studied catalysts. Having the highest strong acid site strength density, the Pt NPs-supported O-OMC catalyst exhibited the highest selectivity toward the dehydrocyclization of *n*-heptane into toluene formation, with 22% selectivity at the same reaction conditions.

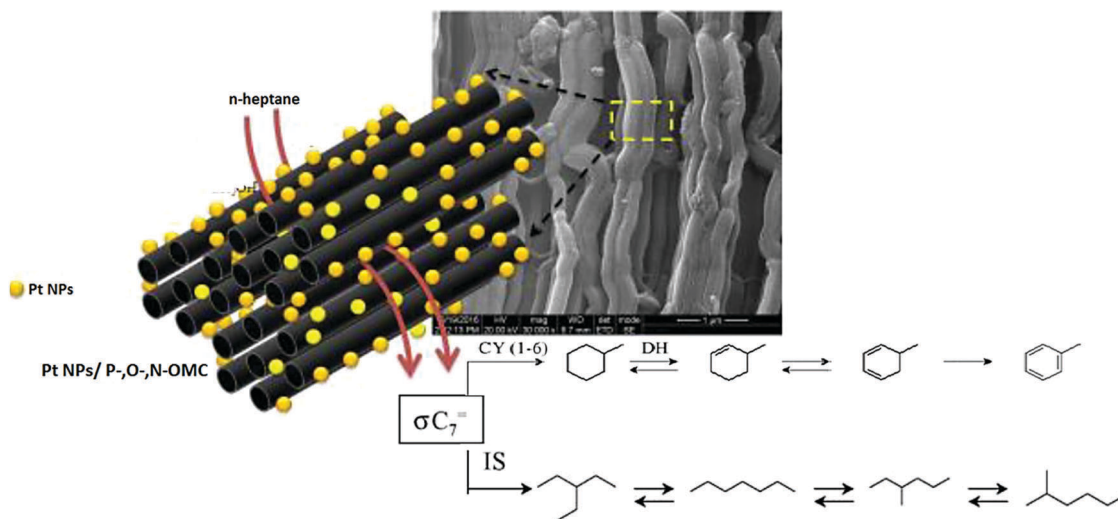
The histogram in Fig. 13B displays the ratio between isomerization and the sum of cyclization + dehydrocyclization (IS/Cy + DCy) products at the same reaction temperature, 350 °C, and at total conversion of ~6.7%, 5.8%, and 3.1% for the Pt NPs-supported P-OMC, O-OMC, and N-OMC studied catalysts, respectively. As shown, all the bifunctional catalysts emphasized different (IS/Cy + DCy) ratio value magnitudes; the highest value was obtained for both the Pt NPs-supported N-OMC and O-OMC catalyst samples and particularly for the Pt NPs-supported N-OMC, indicating the dominancy of isomerization products over the cyclization + dehydrocyclization reactions. On the other hand, the lowest value was observed over the Pt NPs-supported P-OMC bifunctional catalyst, highlighting the fast desorption of cyclization + dehydrocyclization over isomerization reactions. These differences may be explained in terms of the variation of the acid site strength of the catalysts; particularly, the presence of more weak acid sites is necessary for achieving high catalytic activity in isomerization reactions.

4.2. Mechanistic proposal for *n*-heptane hydroconversion

From the identified converted product resulting from the hydroconversion of *n*-C₇ analyzed above, one can conclude that *n*-heptane was transformed over the Pt NPs-supported P-OMC, N-OMC, and O-OMC catalysts following consecutive and parallel interconnected different reactions, namely, isomerization (IS), cyclization (CY), and dehydrocyclization (DCY) as proposed in Scheme 1.

The adsorption of carbon atoms on Pt NPs metal led to the formation of a heptene-like intermediate ($=C_7$), in agreement with most of the published results.⁴⁹ This species may be transformed in the following pathways:

(i) Cyclization with C₁–C₆ ring closure on the medium-strength acid sites of the carbon support forming methylcyclohexane, which may desorb to the product phase or successively be dehydrogenated



Scheme 1 Reaction pathway of *n*-heptane hydroconversion.⁵⁰

by Pt NPs metal on the surface and irreversibly transformed into toluene (Scheme 1). This path is very likely, as the appearance of methylcyclohexane as a primary product suggests that it is formed directly from the cyclization of *n*-heptane through a C₁-C₆ ring closure skeletal rearrangement on the acid sites of the carbon support, which is favored over platinum metal sites⁵⁰ and due to the high toluene selectivity over the Pt NPs-supported P-OMC, N-OMC, and O-OMC catalysts, respectively.

(ii) The (=C₇) undergoes skeletal rearrangement with a bond shift isomerization reaction into *i*-C₇ that requires only weak acid site strength.

5. Conclusions

The synthesized P-, N-, and O-OMC support sample characterization analysis assured that the structural and the morphological aspects of the SBA-15 silica hard template were faithfully transferred to mesoporous carbons by a successful replication process. Here, 10 wt% Pt NPs were loaded on to P-, N-, and O-OMC supports with the aid of the ethylene glycol (EG) reduction method, where the detection of Pt metal (Pt(0)) NPs having a face-centered cubic (fcc) crystal phase structure, revealed the accomplished Pt deposition to its metal state by the EG reduction method. The Pt NPs/P-, N-, and O-OMC samples were analyzed by various spectroscopic techniques and the results emphasized the outstanding roles of nitrogen and oxygen functionalities on the OMC surface in terms of the following:

- Enhancement of Pt NPs dispersion by providing π bonding, which act as anchoring sites for the metallic Pt NPs. Pt NPs dispersion increased from 20% on P-OMC to 45% on the N-OMC support.

- Increased the total acid sites density and variation in the acid site strength.

- Pt NPs were ideally decorated on the ordered array of mesoporous carbon rods of N- and O-OMC samples, whereas they formed large clusters on the surface of P-OMC, as assessed by FE-SEM.

- Decreased the average size of the Pt NPs metal particles from 57 nm on P-OMC to 25 nm on the N-OMC sample.

The catalytic activities of PtNPs/P-, N-, and O-OMCs catalysts were tested for *n*-heptane hydroconversion at a reaction temperature range of 300–500 °C, and H₂/*n*-C₇ of 14 using a fixed-bed flow system operated under atmospheric pressure. All the catalysts displayed identical converted products composed of *i*-C₇, methyl cyclohexane and toluene, ensuring the occurrence of parallel and consecutive interconnected cyclization (CY), dehydrocyclization (DCY), and isomerization (IS) reactions of *n*-heptane hydroconversion over the Pt NPs-supported various OMCs catalysts. A high catalytic activity in terms of *n*-heptane hydroconversion was obtained over the Pt NPs/P- and O-OMC catalysts, which was correlated with the more medium-strength acid sites density, which is essential for activation of the *n*-heptane reactant. On the other hand, a high selectivity toward *i*-C₇ yield formation was attained over the Pt NPs/N-OMC catalyst, establishing a proper balance between the Pt NPs metals dispersion degree and the more weak acid sites density over this catalyst. The value of the IS/Cy + DCy was high for the Pt NPs/N- and O-OMC catalysts compared to that of Pt NPs/P-OMC under the same reaction conditions, demonstrating the positive effect of functionalization of the OMC surface on obtaining isomers that are more valuable products than methyl cyclohexane and toluene products.

Conflicts of interest

There are no conflicts to declare.

Acknowledgements

This research was supported by the Egyptian Petroleum Research Institute (EPRI).

References

- H. Weyda and E. Köhler, *Catal. Today*, 2003, **81**, 51.
- D. Liu, X.-Y. Quek, Sh. Hu, L. Li, H.-M. Lim and Y. Yang, *Catal. Today*, 2009, **147S**, S51–S57.
- R. Ryoo, S. H. Joo and S. Jun, *J. Phys. Chem. B*, 1999, **103**, 7743–7746.
- D. S. Su, S. Perathoner and G. Centi, *Chem. Rev.*, 2013, **113**, 5782–5816.
- X. C. Zhao, A. Q. Wang, J. W. Yan, G. Q. Sun, L. X. Sun and T. Zhang, *Chem. Mater.*, 2010, **22**, 5463–5473.
- Á. Sánchez-Sánchez, F. Suárez-García, A. Martínez-Alonso and J. M. D. Tascón, *J. Colloid Interface Sci.*, 2015, **450**, 91–100.
- C. D. Liang, Z. J. Li and S. Dai, *Angew. Chem., Int. Ed.*, 2008, **47**, 3696–3717.
- J. Jin, N. Nishiyama, Y. Egashira and K. Ueyama, *Microporous Mesoporous Mater.*, 2009, **118**, 218–223.
- A. Stein, Z. Wang and M. A. Fierke, *Adv. Mater.*, 2009, **21**, 265–293.
- M. Barczak, K. Michalak-Zwierz, K. Gdula, K. Tyszczyk-Rotko, R. Dobrowolski and A.-D. Browski, *Microporous Mesoporous Mater.*, 2015, **211**, 162–173.
- J. P. Paraknowitsch and A. Thomas, *Energy Environ. Sci.*, 2013, **6**, 2839–2855.
- P. Singh, S. Campidelli, S. Giordani, D. Bonifazi, A. Bianco and M. Prato, *Chem. Soc. Rev.*, 2009, **38**, 2214–2230.
- Sh.-H. Liu and J.-R. Wu, *Int. J. Hydrogen Energy*, 2012, **37**(7), 16994–17001.
- B. R. Wu and N. F. Zheng, *Nano Today*, 2013, **8**, 168–197.
- M. Zhang, Y. H. Zhao, L. Yan, R. Peltier, W. L. Hui, X. Yao, Y. L. Cui, X. F. Chen, H. Y. Sun and Z. K. Wang, *ACS Appl. Mater. Interfaces*, 2016, **8**, 8834–8840.
- G.-f. Long, X.-h. Lia, K. Wana, Z.-x. Liang, J.-h. Piao and P. Tsiakaras, *Appl. Catal., B*, 2017, **203**, 541–548.
- S. Fernandes, M. Andrade, C. O. Ania, A. Martins, J. Pires and A. P. Carvalho, *Microporous Mesoporous Mater.*, 2012, **163**, 21–28.
- D. Zhao, Q. Huo, J. Feng, B. F. Chmelka and G. D. Stucky, *J. Am. Chem. Soc.*, 1998, **120**, 6024.
- K. S. Lakhi, W. S. Cha, J.-H. Choy, M. Al-Ejji, A. M. Abdullah, A. M. Al-Enizi and A. Vinu, *Microporous Mesoporous Mater.*, 2016, **233**, 44–52.
- C. Ananda, S. V. Priyaa, G. Lawrencea, G. P. Manec, D. S. Dhawalea, K. S. Prasada, V. V. Balasubramanianb, M. A. Wahaba and A. Vinu, *Catal. Today*, 2013, **204**, 164–169.
- G.-f. Long, X.-h. Li, K. Wan, Z.-x. Liang, J.-h. Piao and P. Tsiakaras, *Appl. Catal., B*, 2017, **203**, 541–548.
- C. Pedrero, T. Waku and E. Iglesia, *J. Catal.*, 2004, **233**, 242–255.
- A. Vinu, *Adv. Funct. Mater.*, 2008, **18**, 816–827.
- S. Jun, S. H. Joo, R. Ryoo, M. Kruk, M. Jaroniec, Z. Liu, T. Ohsuna and O. Terasaki, *J. Am. Chem. Soc.*, 2000, **122**, 10712.
- J. Chen, J. Yang, G. He, X. Hu, Z. Li, S. Shen, M. Radosz and M. Fan, *ACS Sustainable Chem. Eng.*, 2016, **4**, 1439–1445.
- K. N. Kudin, B. Ozbas, H. C. Schniepp, R. K. Prudhomme, I. A. Aksay and R. Car, *Nano Lett.*, 2008, **8**, 36.
- G. Wang, W. Xing and S. Zhuo, *Electrochim. Acta*, 2013, **92**, 269.
- B. Fang, M.-S. Kim, J. H. Kim, S. Lim and J.-S. Yu, *J. Mater. Chem.*, 2010, **20**, 10253.
- W. Chaikittisilp, M. Hu, H. Wang, H.-S. Huang, T. Fujita, K. C. W. Wu, L.-C. Chen, Y. Yamauchi and K. Ariga, *Chem. Commun.*, 2012, **48**, 7259–7261.
- E. E. Pérez-Ramírez, G. de la Rosa-Alvarez, P. Salas, C. Velasco-Santos and A. L. Martínez-Hernández, *Environ. Eng. Sci.*, 2015, **32**, 872–880.
- A. Vinu, P. Srinivasu, M. Takahashi, T. Mori, V. V. Balasubramanian and K. Ariga, *Microporous Mesoporous Mater.*, 2007, **100**, 20–26.
- H. M. Gobara, *Egypt. J. Pet.*, 2012, **21**, 1–10.
- Z. X. Wu, P. A. Webley and D. Y. Zhao, *Langmuir*, 2010, **26**, 10277–10286.
- A. B. Fuertes, *Microporous Mesoporous Mater.*, 2004, **67**, 273–281.
- T. Onfroy, F. Guenneau, M. A. Springuel-Huet and A. Gédéon, *Carbon*, 2009, **47**, 2352–2357.
- V. Mahdavi and M. Mardani, *Mater. Chem. Phys.*, 2015, **155**, 136–146.
- Y. F. Jia and K. M. Thomas, *Langmuir*, 2000, **16**, 1118.
- J. W. Shim, S. J. Park and S. K. Ryu, *Carbon*, 2001, **39**, 1635.
- D. Stéfani, A. J. Paula, B. G. Vaz, R. A. Silva, N. F. Andrade, G. Z. Justo, C. V. Ferreira, A. G. S. Filho, M. N. Eberlin and O. L. Alves, *J. Hazard. Mater.*, 2011, **189**, 391–396.
- A. M. T. Silva, B. F. Machado, J. L. Figueiredo and J. L. Faria, *Carbon*, 2009, **47**, 1670–1679.
- R. Nie, H. Jiang, X. Lu, D. Zhou and Q. Xia, *Catal. Sci. Technol.*, 2016, **6**, 1913–1920.
- Y. Otake and R. G. Jenkins, *Carbon*, 1993, **31**, 1099.
- W. Zhangxiong, A. W. Paul and Z. Dongyuan, *Langmuir*, 2010, **26**(12), 10277–10286.
- G. Tremblay, F. J. Vastola and P. L. Walker, *Carbon*, 1978, **16**, 35.
- G. C. Torres, E. L. Jablonski, G. T. Baronetti, A. A. Castro, S. R. Miguel, O. A. Scelza, M. D. Blanco, M. A. Peña Jiménez and J. L. G. Fierro, *Appl. Catal., A*, 1997, **161**, 213–226.
- A. C. Ferrari, J. C. Meyer, V. Scardaci, C. Casiraghi, M. Lazzeri, F. Mauri, S. Piscanec, D. Jiang, K. S. Novoselov, S. Roth and A. K. Geim, *Phys. Rev. Lett.*, 2006, **97**, 187401.
- D. Liu, Sh. Hu, R. Lau, A. Borgna, G. L. Haller and Y. Yang, *Chem. Eng. J.*, 2009, **151**, 308–318.
- I. E. Maxwell, *Catal. Today*, 1987, **1**, 385.
- D. S. Lafyatis, G. F. Froment, A. Pasaclaerbout and E. G. Derouane, *J. Catal.*, 1994, **147**, 552.
- A. Arcoya, X. L. Seoane and J. M. Grau, *Appl. Catal., A*, 2005, **284**, 85–95.